*nanomaterials*

MDPI

*Article*

# Production of $H_2$-Free Carbon Monoxide from Formic Acid Dehydration: The Catalytic Role of Acid Sites in Sulfated Zirconia

**Hyun Ju Lee [1,†], Dong-Chang Kang [2,†], Eun-Jeong Kim [3], Young-Woong Suh [4], Dong-Pyo Kim [2], Haksoo Han [1,*] and Hyung-Ki Min [5,*]**

[1] Department of Chemical and Biomolecular Engineering, Yonsei University, Seoul 03722, Korea
[2] Department of Chemical Engineering, Pohang University of Science and Technology (POSTECH), Pohang 37673, Korea
[3] School of Energy and Chemical Engineering, Ulsan National Institute of Science and Technology (UNIST), Ulsan 44919, Korea
[4] Department of Chemical Engineering, Hanyang University, Seoul 04673, Korea
[5] LOTTE Chemical Research Institute, Daejeon 34110, Korea
* Correspondence: hshan@yonsei.ac.kr (H.H.); pulcherrima7@gmail.com (H.-K.M.)
† These authors contributed equally to this work.

**Abstract:** The formic acid ($CH_2O_2$) decomposition over sulfated zirconia (SZ) catalysts prepared under different synthesis conditions, such as calcination temperature (500–650 °C) and sulfate loading (0–20 wt.%), was investigated. Three sulfate species (tridentate, bridging bidentate, and pyrosulfate) on the SZ catalysts were characterized by using temperature-programmed decomposition (TPDE), Fourier-transform infrared spectroscopy (FTIR), and X-ray photoelectron spectroscopy (XPS). The acidic properties of the SZ catalysts were investigated by the temperature-programmed desorption of *iso*-propanol (IPA-TPD) and pyridine-adsorbed infrared (Py-IR) spectroscopy and correlated with their catalytic properties in formic acid decomposition. The relative contributions of Brønsted and Lewis acid sites to the formic acid dehydration were compared, and optimal synthetic conditions, such as calcination temperature and sulfate loading, were proposed.

**Keywords:** sulfated zirconia; formic acid; acidity; dehydration; carbon monoxide



**Citation:** Lee, H.J.; Kang, D.-C.; Kim, E.-J.; Suh, Y.-W.; Kim, D.-P.; Han, H.; Min, H.-K. Production of $H_2$-Free Carbon Monoxide from Formic Acid Dehydration: The Catalytic Role of Acid Sites in Sulfated Zirconia. *Nanomaterials* **2022**, *12*, 3036. https://doi.org/10.3390/nano12173036

Academic Editors: Dominique Agustin and Jana Pisk

Received: 16 August 2022
Accepted: 30 August 2022
Published: 1 September 2022



## 1. Introduction

High-purity carbon monoxide (CO) is an important industrial dry etching gas used for semiconductor production [1]. Generally, CO is obtained from the syngas production processes (i.e., steam methane reforming (SMR) and partial oxidation (POX) of hydrocarbons) combined with various separation technologies, such as cryogenic separation, pressure swing adsorption (PSA), and membrane separation. However, producing high-purity CO (>99.995%) by using the aforementioned technologies is practically difficult, owing to the presence of gaseous impurities in syngas, such as methane ($CH_4$), nitrogen ($N_2$), carbon dioxide ($CO_2$), oxygen ($O_2$), and moisture, which cannot be easily separated [2]. In addition, the formation of volatile metal carbonyl impurities ($Fe(CO)_5$ and $Ni(CO)_4$) with ppb-level under high temperature and pressure gives detrimental effects on the quality of semiconductor products. Decomposition of refined formic acid ($CH_2O_2$) to CO and $H_2O$ is an alternative to producing high-purity CO, and this process does not involve interference from impurity gases (i.e., $CH_4$, $N_2$, and $O_2$) and formation of metal carbonyls [3].

Depending on the type of catalyst, the catalytic decomposition of formic acid proceeds via two different routes: dehydration (Equation (1)) to CO and $H_2O$ over acidic catalysts, and dehydrogenation (Equation (2)) to $H_2$ and $CO_2$ over metal or basic catalysts [4–6]. To date, dehydrogenation of formic acid has been more intensively studied than dehydration as a means of hydrogen storage and carriers [7–10]. However, the $H_2$-free dehydration

of formic acid in Equation (1) is essential for producing high-purity CO, whereas with regard to Equation (2), producing $CO_2$ and $H_2$ is an undesirable reaction that must be suppressed [11]. In the dehydration pathway, the conversion of formic acid generally increases proportionally to the concentration of Brønsted acid sites in the catalysts [12]:

$$HCOOH \leftrightarrow CO + H_2O \ (\triangle H^\circ_{298} = 29.20 \text{ kJ mol}^{-1}) \quad (1)$$

$$HCOOH \leftrightarrow CO_2 + H_2 \ (\triangle H^\circ_{298} = 31.20 \text{ kJ mol}^{-1}) \quad (2)$$

Zirconia ($ZrO_2$) is a unique metal oxide that is widely used as a catalyst or support in various applications, owing to its excellent thermal stability and controllable acidic and basic properties [13–16]. Although pure $ZrO_2$ is Lewis acidic, many attempts have been made to increase its Brønsted acidity, such as the addition of acidic metal oxides and sulfate ions. As reported by Lee et al., the addition of $WO_3$ enhances the Brønsted acidity of $ZrO_2$, resulting in an increase in the catalytic activity for formic acid dehydration [17]. Oki et al. successfully increased the Brønsted acidity of $ZrO_2$ by introducing $MoO_3$ and obtained high catalytic activity for the polyesterification of adipic acid with 1,4-butanediol [18]. In the $Cr_2O_3$-$ZrO_2$ system, the nature of the acid sites can be controlled by applying different precursors; that is, $Cr_2O_3$ from ammonium chromate generates Brønsted acid sites, while chromium nitrate leads to the formation of Lewis acid sites [19]. Sulfated zirconia (SZ), which is activated by various sulfating agents, such as $H_2SO_4$, $(NH_4)_2SO_4$, and $H_2S$, is a class of solid superacids exhibiting outstanding catalytic performance for a variety of organic synthesis and transformation reactions, such as alkylation, condensation, and dehydration [20–23]. Niwa et al. successfully measured the concentration of Brønsted and Lewis acid sites in SZ catalysts by using the ammonia infrared-mass spectroscopy/temperature-programmed desorption (IRMS–TPD) method [24]. The generation of strong Brønsted acid sites in the SZ catalysts is suggested to be primarily responsible for their high catalytic activity in *n*-heptane cracking. Furthermore, Huang et al. reported different ratios of Brønsted to Lewis acid sites in sulfated monoclinic and tetragonal zirconia phases—0.50 and 0.55, respectively [25]. However, the physicochemical properties of the SZ catalysts differ significantly from those of the synthesis method, calcination temperature, and sulfate ion precursors [26].

Here, we systematically investigated the effects of the synthetic parameters of SZ catalysts, such as calcination temperature and sulfate ion content, on the decomposition of formic acid. The acidity of SZ was characterized by the temperature-programmed desorption of *iso*-propanol (IPA-TPD) and pyridine-adsorbed infrared (Py-IR) spectroscopy. The relative contributions of the Brønsted and Lewis acid sites to the conversion of formic acid were compared.

## 2. Materials and Methods

### *2.1. Catalyst Preparation*

$Zr(OH)_4$ was synthesized by using zirconyl chloride ($ZrOCl_2 \cdot 8H_2O$, Kanto, 99%) and ammonia solution (28 wt.% $NH_4OH$, SK Chemical). In a typical preparation, aqueous ammonia solution was added dropwise to a 0.5 M zirconyl chloride aqueous solution, under vigorous stirring, until a pH of 9.5 was reached. The resulting suspension was aged at 100 °C for 48 h and subsequently washed with distilled water until the pH of the filtrate reached 7.0, thereby confirming the complete removal of residual $Cl^-$ ions. Finally, a $Zr(OH)_4$ cake was recovered and dried at 100 °C for 24 h.

SZ catalysts with different sulfate ion contents (0–20 wt.%) were prepared by using the incipient wetness impregnation method. In a typical preparation, the desired amount of ammonium sulfate ($(NH_4)_2SO_4$, Samchun, 99%) solution as a sulfating agent was added to the $Zr(OH)_4$ powder and dried at 100 °C for 24 h. Finally, the sample was calcined at different temperatures in a range of 500–650 °C for 2 h (ramping rate of 2 °C $min^{-1}$), under ambient air. The catalyst was denoted as *x*SZ(*y*), where *x* and *y* represent the sulfate content and calcination temperature, respectively. For comparison, pure $ZrO_2$ was prepared by

calcination of $Zr(OH)_4$ at 600 °C for 2 h without an addition of $(NH_4)_2SO_4$ and was denoted as 0SZ(600).

### 2.2. Characterization of Catalysts

Powder X-ray diffraction (XRD) analysis was performed on a D8 Discover (Bruker AXS, billericay, MA, USA), using Cu K$\alpha$ radiation ($\lambda$ = 0.15468 nm) in the 2$\theta$ range of 10–80° (scan rate = 0.009° $s^{-1}$). The crystal structures of the catalysts were analyzed by using the Joint Committee on Powder Diffraction Standards (JCPDS) database. The specific surface area and pore size were measured by $N_2$ sorption at −198 °C, using an ASAP2020 gas adsorption analyzer (Micromeritics, Norcross, GA, USA). Prior to the measurement, all samples were degassed at 250 °C for 4 h, under vacuum, and the surface area was determined by using the Brunauer–Emmett–Teller (BET) method from the relative pressure ($P/P_0$), ranging from 0.05 to 0.20. The morphology of the catalysts was investigated by scanning electron microscopy (SEM), using an LEO-1530 microscope (Carl Zeiss, Oberkochen, Germany). The sulfate ion content was determined by using an elemental analyzer (Elementar vario MACRO cube, Langenselbold, Germany) and energy-dispersive X-ray spectroscopy (EDS, Carl Zeiss, Libra 120). Thermogravimetric analysis (TGA) was conducted on an SDT Q600 (TA Instruments) in temperatures ranging from 100 to 1000 °C (ramping rate of 10 °C $min^{-1}$), under a flowing $N_2$ (100 $cm^3$ $min^{-1}$) atmosphere. Fourier-transform infrared (FTIR) spectra were recorded on an IFS 66/S spectrometer (Bruker Optic Gmbh, Ettlingen, Germany) in the range of 400–4000 $cm^{-1}$, with a resolution of 2 $cm^{-1}$. The temperature-programmed decomposition (TPDE) experiment was performed by using a home-built apparatus with a mass spectrometer detector (Blazers QMS200, Nashua, NH, USA). Typically, ca. 0.05 g catalyst fixed in a U-shaped quartz reactor is heated from room temperature (RT) to 1000 °C (ramping rate of 10 °C $min^{-1}$), under an Ar atmosphere. The IPA-TPD experiment was also conducted on the same apparatus as the TPDE, using a similar procedure. Here, a ca. 0.05 g of sample was pretreated at 300 °C for 1 h, under flowing Ar (30 $cm^3$ $min^{-1}$), exposed to 3% IPA (30 $cm^3$ $min^{-1}$, balanced with Ar) flow for 0.5 h at RT, and subsequently purged with flowing Ar (30 $cm^3$ $min^{-1}$) for 0.5 h to remove the physically adsorbed IPA on the catalyst's surface. The IPA-TPD profile was measured by heating the sample from RT to 400 °C (ramping rate = 10 °C $min^{-1}$), and the mass signal corresponding to $m/z$ = 41 ($C_3H_5$) was recorded. Py-IR spectra were obtained on a Thermo Nicolet 6700 (Thermo Fisher Scientific, Waltham, MA, USA) by using self-supporting catalyst wafers of approximately 30 mg (1.3 cm diameter). Prior to the measurements, the catalyst wafers were pretreated under vacuum at 300 °C for 1 h inside a home-built IR cell with ZnSe windows, exposed to 64 µmol of pyridine at 150 °C, and then evacuated at the same temperature to remove the physisorbed pyridine. IR spectra were collected at 150 °C (32 scans with a resolution of 4 $cm^{-1}$), and the concentrations of Brønsted and Lewis acid sites were calculated from the intensities of the IR bands at approximately 1550 and 1450 $cm^{-1}$, respectively, using the molar extinction coefficients reported by Emeis [27]. X-ray photoelectron spectroscopy (XPS) was performed on a PHI Quantera-II (Ulvac-PHI, Chigasaki, Kanagawa, Japan) instrument with monochromatic Al-K$\alpha$ radiation ($h\nu$ = 1486.6 eV). XPS data were calibrated by referencing the binding energy of adventitious carbon (C 1 s, 284.6 eV) as the standard. All spectral deconvolutions were performed by using Origin 9.0, a curve-fitting function.

### 2.3. Activity Test

The performance of the SZ catalyst was measured in a fixed-bed quartz reactor, under atmospheric pressure. Prior to the test, ca. 0.1 g of the catalyst was routinely activated under flowing Ar (100 $cm^3$ $min^{-1}$) at 400 °C for 1 h and then cooled to the reaction temperature (260 °C). Isothermal activity tests were performed by introducing 5% formic acid (balanced with Ar) at a total flow rate of 100 $cm^3$ $min^{-1}$. The reactor effluent was analyzed online by using a gas chromatograph (CP 3800, Varian) equipped with a Proapak Q column (1.8 m

length and 1/8″ o.d.) and a thermal conductivity detector (TCD). Formic acid conversion was calculated by using the following equation:

$$\text{Conversion } (\%) = \frac{F_{HCOOH\ in} - F_{HCOOH\ out}}{F_{HCOOH\ in}} \times 100$$

where $F_{HCOOH\ in}$ and $F_{HCOOH\ out}$ are the molar flow rates of formic acid at the inlet and outlet, respectively. The selectivity for CO was 100%, and $CO_2$ formation was not observed for any of the SZ catalysts used in this study. The carbon balance over all catalysts employed in this study was 100%.

## 3. Results and Discussion

### *3.1. Physicochemical Properties of SZ Catalysts*

Figure 1a shows the XRD patterns of the 5SZ(*y*) catalysts calcined at different temperatures (*y* = 500–650 °C). All the catalysts exhibited a tetragonal crystalline phase (JCPDS No. 50–1089). Furthermore, peaks corresponding to the monoclinic crystalline phase (JCPDS No. 37–1484) were not detected. Although the crystallinity of 5SZ(500) was very low owing to the insufficient temperature to crystallize $ZrO_2$, a fully crystallized tetragonal phase was observed in the 5SZ(600) and 5SZ(650) catalysts, indicating that a temperature higher than 600 °C is required to completely crystallize the SZ catalysts. Ward and Ko also reported a similar temperature of 500 °C to crystallize 5 mol% SZ and found that the crystallization temperature of this material increased with sulfate loading [28]. However, the BET surface areas of the 5SZ catalysts continuously decreased from 234 to 145 $m^2\ g^{-1}$ as the calcination temperature increased from 500 to 650 °C (Table 1). This surface-area loss was accompanied by an increase in particle size (3.8 → 7.0 nm) calculated by the Scherrer equation, representing the sintering of $ZrO_2$ crystals during the crystallization process, which was further confirmed by SEM analysis (Supplementary Figure S1). However, the pore sizes of the 5SZ(*y*) catalysts, as shown in Supplementary Figure S2, were slightly increased from 8.3 to 8.7 nm, owing to the crystallized tetragonal phase [29,30]. From the EDS image of the 5SZ(600) catalyst, a uniform distribution of sulfate species on the surface of $ZrO_2$ was identified (Supplementary Figure S3). The sulfate ion contents in 5SZ(*y*), as measured by elemental analysis, decreased from 4.8 to 3.5 wt.% with an increase in the calcination temperature, owing to the partial decomposition of sulfate ion to $SO_2$ and $O_2$. The sulfate ion contents in the 5SZ(*y*) catalysts were matched with the weight losses calculated from the TGA experiments, as shown in Supplementary Figure S4a. In the TGA analysis, the weight loss below 600 °C corresponds to the desorption of physically adsorbed water molecules and dihydroxylation of surface hydroxyl groups, and that observed at higher temperatures (>600 °C) is attributed to the thermal decomposition of sulfate species [31,32]. The sulfate ion density, defined as the number of sulfate ions per $nm^2$ on the surface of the 5SZ(*y*) catalysts, ranged from 1.3 to 1.5.

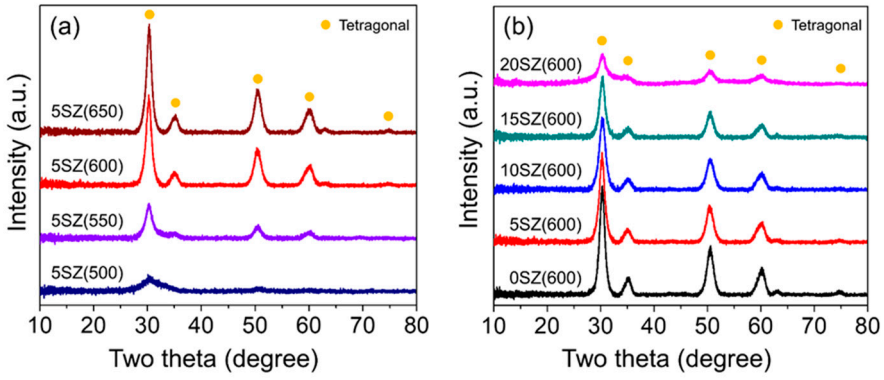


**Figure 1.** XRD patterns of (**a**) 5SZ(*y*) and (**b**) *x*SZ(600) catalysts prepared by using different calcination temperatures and the sulfate contents, respectively.

**Table 1.** Physicochemical properties of *x*SZ(*y*) catalysts.

| Catalyst | Particle Size [1] (nm) | $S_{BET}$ ($m^2$ $g^{-1}$) | Pore Size [2] (nm) | $SO_4^{2-}$ Content [3] (wt.%) |
|---|---|---|---|---|
| 5SZ(500) | 3.8 | 234 | 8.3 | 4.8 (1.3) |
| 5SZ(550) | 5.2 | 205 | 8.3 | 4.3 (1.3) |
| 5SZ(600) | 6.3 | 165 | 8.7 | 4.0 (1.5) |
| 5SZ(650) | 7.0 | 145 | 8.7 | 3.5 (1.5) |
| 0SZ(600) | 6.5 | 142 | 10.3 | - |
| 5SZ(600) | 6.3 | 165 | 8.7 | 4.0 (1.5) |
| 10SZ(600) | 6.0 | 172 | 8.7 | 6.1 (2.2) |
| 15SZ(600) | 5.9 | 151 | 7.7 | 9.5 (4.0) |
| 20SZ(600) | 5.5 | 141 | 6.9 | 12.6 (5.6) |

[1] Calculated from Scherrer's equation at $2\theta = 30.3°$. [2] Pore size determined at the maximum of pore size distribution calculated by the Barrett–Joyner–Halenda (BJH) method from the desorption branch. [3] $SO_4^{2-}$ content evaluated from the S content in the elemental analysis. The values in parentheses denote sulfate density ($SO_4^{2-}$ ions $nm^{-2}$).

As shown in Figure 1b, the crystallinity of *x*SZ(600) catalysts steadily decreased as the sulfate ion loading (*x* = 0, 5, 10, 15, and 20) in SZ increased. However, XRD peaks other than those corresponding to the tetragonal phase were not observed. Notably, the BET surface areas of *x*SZ(600) catalysts showed a volcano-shaped distribution with respect to the sulfate ion content, exhibiting a maximum value (172 $m^2$ $g^{-1}$) at 10 wt.% loading. The decrease in the BET surface area for the *x*SZ(600) samples with *x* = 15 and 20 can be explained by the formation of polysulfate species, such as pyrosulfate, partially blocking the pores of $ZrO_2$ [33,34]. Unlike that of 5SZ(y), the particle size and pore size of the *x*SZ(600) catalysts continuously decreased as the sulfate ion content increased (Supplementary Figure S5); this outcome can be attributed to the decrease in the XRD peak intensity of the tetragonal phase, as shown in Figure 1. This retardation of crystallization by the addition of sulfate ions was also reported by Ward and Ko [28]. The sulfate ion contents in *x*SZ(600) catalysts increased from 4.0 to 12.6 wt.%, and the sulfate densities were proportionally increased from 1.5 to 5.6 $SO_4^{2-}$ ions per $nm^2$ by adding sulfate species. The much higher weight loss (ca. 9.9 wt.%) observed for 20SZ(600) than for other catalysts shown in Supplementary Figure S4b also supported the presence of massive sulfate species in this catalyst. As reported by Katada et al., a monolayer of sulfate species on the $ZrO_2$ surface was formed at 3.2 $SO_4^{2-}$ ions per $nm^2$ by applying its kinetic diameter [35]. Bensitel et al. and Morterra et al. reported that the transition of isolated sulfate ions to polysulfate species occurs at sulfate ion densities higher than 1.5 $SO_4^{2-}$ ions per $nm^2$ [36,37]. Thus, the formation of multilayer sulfate or polysulfate species on *x*SZ(600) catalysts can be expected for sulfate contents higher than 15 wt.% (*x* > 15).

The sulfate species on $ZrO_2$ were characterized by tracing the mass signal of the $\cdot SO_2$ fragment (*m*/*z* = 64) during the TPDE experiment (Figure 2 and Table 2). Deconvolution of the mass signals shown in Figure 2 generated three different peaks with respect to the decomposition temperatures: 700 (Peak I), 713 (Peak II), and 815 °C (Peak III). Although Peak III prevailed across samples, Peak I was observed for the 5SZ(*y*) samples calcined at relatively low temperatures (i.e., 5SZ(500) and 5SZ(550)), owing to the weak interaction of sulfate species with the amorphous $ZrO_2$ domain. Furthermore, Glover et al. reported the low-temperature (600−700 °C) decomposition of sulfate species on the $Zr(OH)_4$ surface [38]. As shown in Supplementary Figure S6, the TPDE of the as-prepared 10SZ catalyst produced $\cdot SO_2$ and a small number of ·NH (*m*/*z* = 15) fragments at 700 °C. Thus, the decomposition of ammonium pyrosulfate ($(NH_4)_2S_2O_7$), a major compound produced during the decomposition of $(NH_4)_2SO_4$, cannot be ruled out [39]. However, these peaks completely disappeared for 10SZ(600), and the evolution of only the $\cdot SO_2$ fragment at 850 °C was observed. The three representative conformations of the surface-bound sulfate species on $ZrO_2$ are illustrated in Scheme 1 [40,41]. Here, tridentate (Type I) and bridging bidentate (Type II) species were reported to be the most stable, decomposing at temperatures higher than 800 °C [42]. Considering that the Type I conformation is a dehydrated form of Type II,

·$SO_2$ desorption at 815 °C can be attributed to the decomposition of Type I species [43]. As shown in Figure 2b, Peak II, which is centered at 713 °C, was observed in the samples with high sulfate content (>15 wt.%), that is, 15SZ(600) and 20SZ(600). This can be rationalized by the formation of new surface sulfoxy species (Type III in Scheme 1) at high sulfate loadings, which are more easily decomposed in the lower temperature region. Rabee et al. observed the generation of an $SO_2$ fragment at 670 °C for the SZ catalysts with high sulfate content owing to the decomposition of pyrosulfate anions ($S_2O_7^{2-}$) [42].

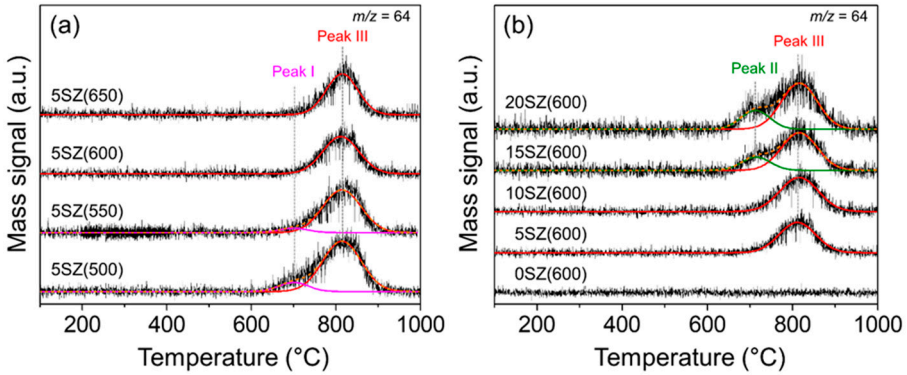


**Figure 2.** Evolution of·$SO_2$ (*m*/*z* = 64) in mass spectra as a function of decomposition temperature during TPDE experiment over (**a**) 5SZ(*y*) and (**b**) *x*SZ(600) catalysts.

**Table 2.** Results of TPDE, IPA-TPD, and Py-IR over *x*SZ(*y*) catalysts.

| Catalyst | TPDE | | | Py-IR | | IPA-TPD |
|---|---|---|---|---|---|---|
| | $T_{max, 64}$ [1] (°C) | | | Acid Site Density [2] (μmol $m^{-2}$) | | $T_{max, 41}$ [3] (°C) |
| | Peak I | Peak II | Peak III | Lewis Acid | Brønsted Acid | |
| 5SZ(500) | 700 (12) [4] | 814 (88) | - | 0.59 | 0.09 | 155 |
| 5SZ(550) | 700 (7) | 814 (93) | - | 0.62 | 0.16 | 139 |
| 5SZ(600) | - | 814 (100) | - | 0.62 | 0.32 | 126 |
| 5SZ(650) | - | 814 (100) | - | 0.61 | 0.05 | 128 |
| 0SZ(600) | - | - | - | 0.46 | - | 235 |
| 5SZ(600) | - | 814 (100) | - | 0.62 | 0.32 | 126 |
| 10SZ(600) | - | 815 (100) | - | 0.78 | 0.66 | 122 |
| 15SZ(600) | - | 816 (78) | 714 (22) | 0.75 | 0.42 | 124 |
| 20SZ(600) | - | 816 (95) | 713 (25) | 0.50 | 0.36 | 129 |

[1] $T_{max, 64}$ is the peak temperature of the ·$SO_2$ (*m*/*z* = 64) evolution in TPDE profile. The values in parentheses denote the proportions of Peaks I, II, and III, based on the integrated area. [2] Acid site density calculated from the peak areas of the absorption band at 1444 $cm^{-1}$ (Lewis acid) and 1540 $cm^{-1}$ (Brønsted acid) following the procedure reported by Emeis and normalized by $S_{BET}$ [27]. [3] $T_{max, 41}$ is the peak temperature of ·$C_3H_5$ (*m*/*z* = 41) evolution in the IPA-TPD profile. [4] The value in parentheses denotes the percentage of each peak.

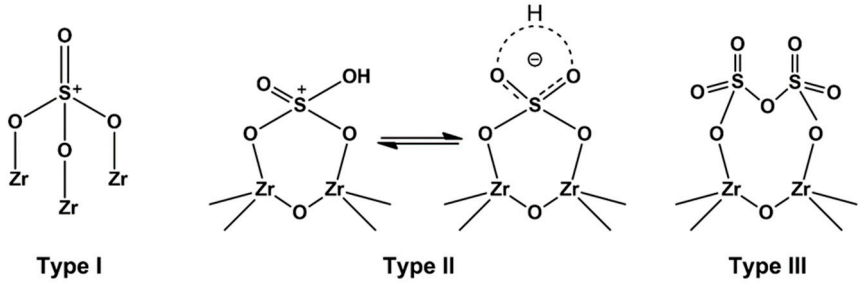


**Scheme 1.** Three different types of sulfate species on SZ catalysts.

The nature of the surface sulfate species on the SZ catalysts was further investigated by using FTIR spectroscopy (Figure 3). Except for 0SZ(600), all SZ catalysts exhibited IR absorption bands from 900 to 1300 $cm^{-1}$, which are characteristic bands of surface sulfate species [44]. The bands at 1130 and 1225 $cm^{-1}$ corresponded to the S=O vibrations in the bridging bidentate sulfate coordinated to $Zr^{4+}$, while those at 995, 1030, and 1076 $cm^{-1}$ corresponded to the S–O stretching vibrations [45,46]. In addition, the band observed at 1628 $cm^{-1}$ was attributed to the bending vibrations of adsorbed water [47]. Notably, the intensity of the bands from S–O stretching vibrations (1030 and 1076 $cm^{-1}$) for the 5SZ(*y*) samples was enhanced with an increase in the calcination temperature owing to the crystallization of the tetragonal $ZrO_2$ phase (Figure 3a). This correlates well with the reduction of adsorbed water (1628 $cm^{-1}$ in Figure 3a and 3700–3200 $cm^{-1}$ in Supplementary Figure S7a) and amorphous $ZrO_2$ phase in XRD patterns (Figure 1a). However, the IR band at ca. 813 $cm^{-1}$, corresponding to Zr–O vibration, was observed in the 5SZ(600) and 5SZ(650) samples, owing to the removal of sulfate species from the $ZrO_2$ surface by high-temperature calcination [48,49]. In contrast, the IR bands corresponding to S=O vibrations (1130 and 1225 $cm^{-1}$) increased for *x*SZ(600) catalysts with an increase in the sulfate content. This is in line with the formation of Types II and III sulfate species derived from the TPDE experiments (Figure 2b). Unlike the continuous increase in S=O vibrations, the intensity of the band at 1628 $cm^{-1}$ was maximized at 10SZ(600) and decreased with further increase in sulfate loading. The same trends were observed in the IR spectra of *x*SZ(600) samples in the hydroxyl region (Supplementary Figure S7b). This can be rationalized by the reaction of two adjacent bidentate species with pyrosulfate anions ($2HSO_4^- \rightarrow S_2O_7^- + H_2O$), releasing a mole of water [50].

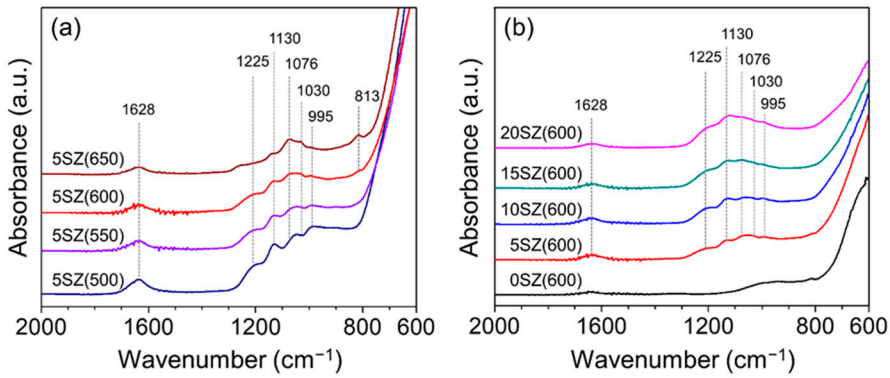


**Figure 3.** FTIR spectra of (**a**) 5SZ(*y*) and (**b**) *x*SZ(600) catalysts prepared at different calcination temperatures and sulfate contents, respectively.

The changes in the chemical states of Zr and S in the SZ catalysts with respect to the calcination temperature and sulfate loading were characterized by XPS (Figure 4 and Table 3). The Zr $3d_{5/2}$ spectra of all catalysts showed two chemical states, namely from 181.9 to 182.5 eV (Peak I) and from 182.9 to 183.6 eV (Peak II), which were assigned to Zr–O and Zr–OH, respectively [51–54]. The S $2p_{3/2}$ peak centered at 169±0.1 eV was assigned to $S^{6+}$ for $SO_4^{2-}$ [55,56]. The O 1s peak in Supplementary Figure S8 was deconvoluted into three peaks, namely 530.0–530.4 eV (Peak I), 531.6–532.2 eV (Peak II), and 533.0 eV (Peak III), arising from the oxygen in Zr–O, Zr–OH, and sulfate species, respectively [57,58]. Notably, the binding energies of Zr $3d_{5/2}$, S $2p_{3/2}$, and O 1s in the 5SZ(*y*) catalysts were almost unchanged with respect to the calcination temperature, representing identical chemical states of Zr, S, and O in these catalysts (Table 3). However, the relative proportion of Peak I (Zr–O) in the Zr $3d_{5/2}$ spectra of the 5SZ(*y*) catalysts increased from 66.7 to 73.5%, owing to the crystallization of amorphous $ZrO_2$ to the tetragonal phase at high temperatures. In addition, in line with the reduction in sulfate content shown in Table 1, the intensity of S $2p_{3/2}$ in the 5SZ(*y*) catalysts was reduced with an increase in the calcination temperature. In the case of *x*SZ(600) catalysts, all binding energies of Zr $3d_{5/2}$, S $2p_{3/2}$, and O 1s were higher

than those of 0SZ(600) and steadily increased with the increase in sulfate loading, owing to the strong interaction between the sulfate species and $ZrO_2$ [59]. Notably, the relative proportion of Zr $3d_{5/2}$ and O 1s peaks centered at 183.2−183.4 eV and 531.7−531.9 eV, respectively, corresponding to Zr–OH species, was maximized on the catalyst with 10 wt.% sulfate loading (10SZ(600)). The highest proportion of Zr–OH on the 10SZ(600) catalyst was also correlated with the highest intensity of the 1628 $cm^{-1}$ band in the FTIR spectrum (Figure 3b).

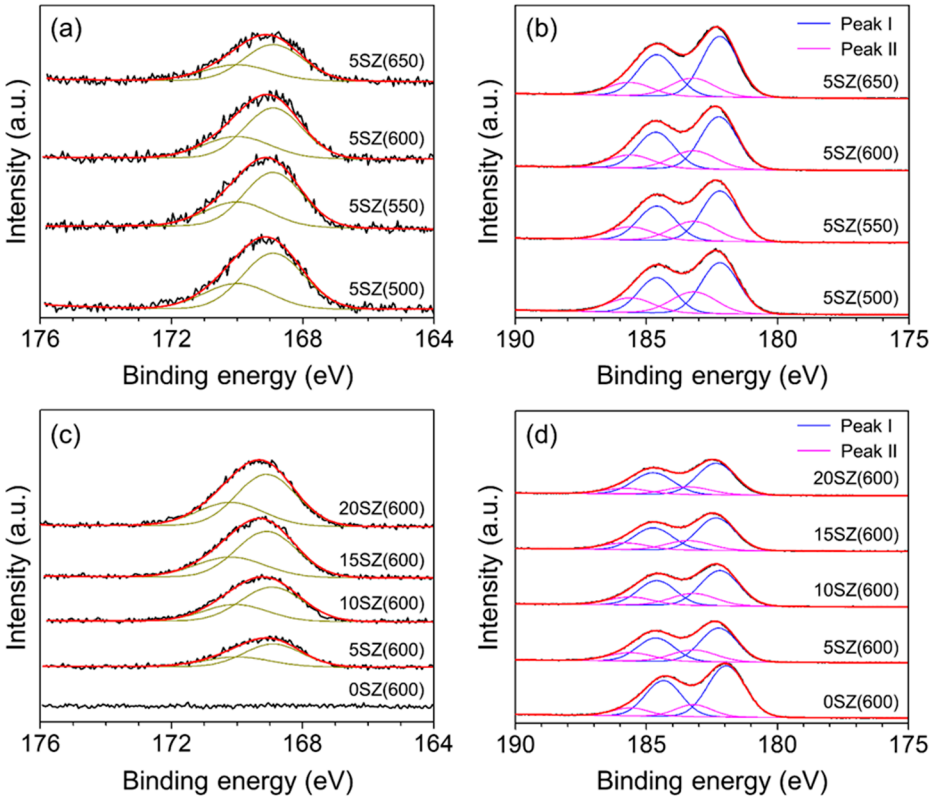


**Figure 4.** Deconvoluted XPS spectra of S $2p_{3/2}$ (**a**,**c**) and Zr $3d_{5/2}$ (**b**,**d**) over *x*SZ(*y*) catalysts.

**Table 3.** Binding energies of the deconvoluted peaks from S $2p_{3/2}$, Zr $3d_{5/2}$, and O 1s XPS spectra.

| Catalyst | Binding Energy (eV) | | | | | |
|---|---|---|---|---|---|---|
| | S $2p_{3/2}$ | Zr $3d_{5/2}$ | | O 1s | | |
| | | Peak I | Peak II | Peak I | Peak II | Peak III |
| 5SZ(500) | 168.9 | 182.2 (66.7) [1] | 183.2 (33.3) | 530.1 (47.9) | 531.6 (36.0) | 533.0 (16.2) |
| 5SZ(550) | 168.9 | 182.2 (68.0) | 183.2 (32.0) | 530.1 (50.6) | 531.6 (33.7) | 533.0 (15.7) |
| 5SZ(600) | 168.9 | 182.2 (70.6) | 183.2 (29.4) | 530.2 (53.0) | 531.6 (31.7) | 533.0 (15.3) |
| 5SZ(650) | 168.9 | 182.2 (73.5) | 183.2 (26.5) | 530.2 (59.4) | 531.7 (28.6) | 533.0 (12.0) |
| 0SZ(600) | - | 182.0 (81.7) | 183.2 (18.3) | 530.0 (77.5) | 530.2 (22.5) | - |
| 5SZ(600) | 168.9 | 182.2 (70.6) | 183.2 (29.4) | 530.2 (53.0) | 531.7 (31.7) | 533.0 (15.3) |
| 10SZ(600) | 168.9 | 182.2 (67.8) | 183.2 (32.2) | 530.2 (47.5) | 531.7 (34.7) | 533.0 (17.7) |
| 15SZ(600) | 169.1 | 182.3 (74.5) | 183.4 (25.5) | 530.4 (51.6) | 531.9 (28.4) | 533.0 (20.0) |
| 20SZ(600) | 169.1 | 182.3 (77.8) | 183.4 (22.2) | 530.4 (51.0) | 531.9 (26.9) | 533.0 (22.1) |

[1] The value in parentheses denotes the percentage of each peak.

The acidic properties of the SZ catalysts were characterized by using IR spectroscopy with pyridine adsorption (Figure 5 and Table 2). The characteristic bands observed at 1444, 1580, and 1610 $cm^{-1}$ correspond to the coordinatively adsorbed pyridine on Lewis acid sites, while the band at 1540 $cm^{-1}$ corresponds to the pyridinium ion on Brønsted acid

sites [60,61]. The concentration of acid sites on the catalysts was calculated by using the integrated area of the bands at 1444 and 1540 $cm^{-1}$ for the Lewis and Brønsted acid sites, respectively, by applying the molar extinction coefficients reported by Emeis and normalized by $S_{BET}$ values [27]. As shown in Table 2, although the densities (0.59−0.62 μmol $m^{-2}$) of Lewis acid sites on 5SZ(*y*) catalysts did not vary considerably in the whole temperature region, those of Brønsted acid sites were linearly increased with calcination temperature up to 600 °C and decreased at the higher temperature. However, the distribution of Lewis acid as well as Brønsted acid densities on *x*SZ(600) catalysts was volcano-shaped with maxima at 0.78 and 0.66 μmol $m^{-2}$, respectively, with 10 wt.% sulfate loading (10SZ(600)). A further increase in the sulfate ions on the SZ catalysts reduced the concentration of acid sites, owing to the transformation of Brønsted acidic bridging bidentate species (Type II) to pyrosulfate-like species, as evidenced by the formation of Peak II in Figure 2b. However, this transformation of Type II bridging bidentate to Type III surface sulfoxy species does not promote the Lewis acidity of catalysts. This is probably caused by the shielding of $ZrO_2$ sites by excessive amounts of sulfoxy species and the reduction of surface areas of catalysts.

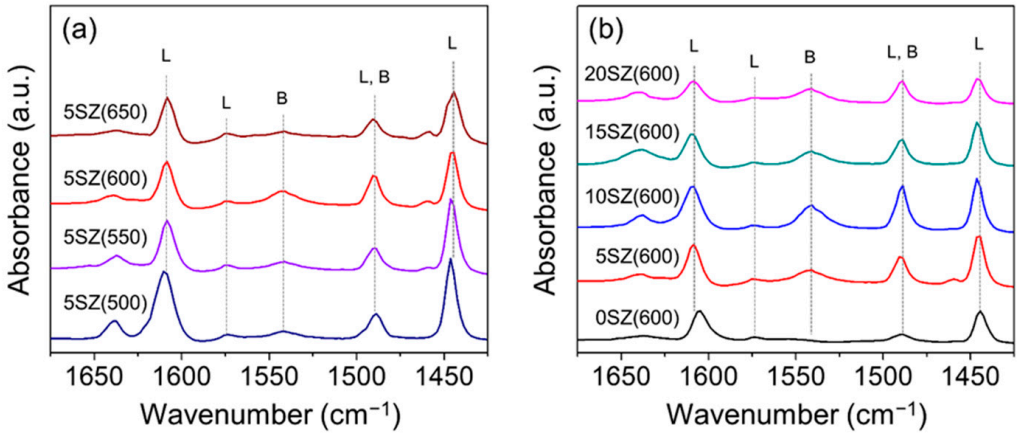


**Figure 5.** Py-IR spectra of (**a**) 5SZ(*y*) and (**b**) *x*SZ(600) catalysts prepared by using different calcination temperatures and the sulfate contents, respectively.

The acid strengths of the SZ catalysts were investigated by using IPA-TPD as a test reaction (Figure 6). Generally, the peak temperature ($T_{max, 41}$) of $\cdot C_3H_5$ (*m*/*z* = 41) desorption originating from IPA dehydration is an indicator of the acid strength [11]. The absence of $\cdot CH_3CO$ (*m*/*z* = 43) fragment on 0SZ(600) during IPA-TPD represents the lack of base sites on this catalyst (Supplementary Figure S9). As shown in Figure 6 and Table 2, the $T_{max, 41}$ of 0SZ(600) was 235 °C, indicating its low acidity and low activity in IPA conversion. However, the lowest $T_{max, 41}$ (126 °C) of $\cdot C_3H_5$ desorption was observed for 5SZ(600) among the 5SZ(*y*) catalysts, implying that this catalyst is highly acidic. This was in good agreement with the highest Brønsted density of 5SZ(600), as shown in Figure 5 and Table 2. Meanwhile, the $T_{max, 41}$ of $\cdot C_3H_5$ desorption on the 5SZ(650) catalyst was slightly increased, implying a reduction in acidity. In the case of *x*SZ(600) catalysts, the lowest $T_{max, 41}$ of $C_3H_5$ desorption was observed for the 10SZ(600) catalyst, which was also correlated with the highest acid densities of both Lewis and Brønsted acids (Figure 5). In line with the decrease in the acid densities for the 15SZ(600) and 20SZ(600) catalysts, an increase in of $T_{max, 41}$ was observed for these catalysts, indicating their reduced acid strength.

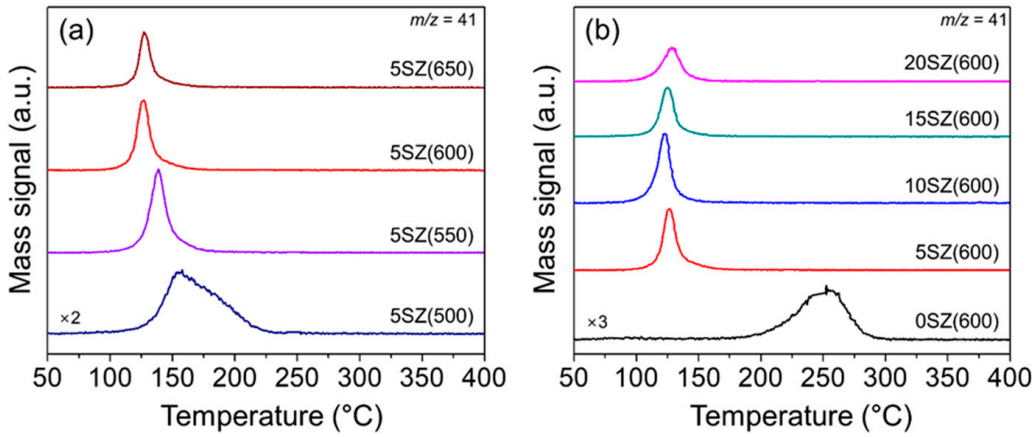


**Figure 6.** Evolution of $\cdot C_3H_5$ ($m/z$ = 41) in mass spectra as a function of desorption temperature during IPA-TPD analysis over (**a**) 5SZ($y$) and (**b**) $x$SZ(600) catalysts.

### *3.2. HCOOH Decomposition*

The catalytic performances of the SZ catalysts for the decomposition of formic acid at 260 °C were compared, as shown in Figure 7. Here, CO was the sole product of all the employed catalysts, with 100% selectivity. As shown in Figure 7a, although steady deactivation was observed for all the 5SZ($y$) catalysts, the conversion of formic acid during the test period decreased in the following order: 5SZ(600) > 5SZ(650) > 5SZ(550) > 5SZ(500). This trend in formic acid conversion over the 5SZ($y$) catalysts was exactly matched with $T_{max,\,41}$ in Table 2, indicating that the strength of the acid sites plays a decisive role in the dehydration of formic acid. As shown in Supplementary Figure S10, 10SZ(600) exhibited the highest formic acid conversion among the 10SZ($y$) catalysts. Thus, the optimal calcination temperature for the SZ catalysts was identified as 600 °C. For the $x$SZ(600) catalysts shown in Figure 7b, the conversion of formic acid was also well correlated with $T_{max,\,41}$ in Table 2 and decreased in the following order: 10SZ(600) > 15SZ(600) > 5SZ(600) $\geq$ 20SZ(600) > 0SZ(600). Unmodified 0SZ(600) exhibited very poor catalytic activity, with a conversion of less than 40%. Unlike the other $x$SZ(600) catalysts, the conversion of formic acid over 10SZ(600) and 15SZ(600) was stabilized after 1 h, and no significant deactivation was observed. The initial conversion of formic acid over $x$SZ($y$) catalysts was plotted as $T_{max,\,41}$ and acid site density (Figure 8). As shown in Figure 8a, the conversion of formic acid over 5SZ($y$) catalysts was inversely related to $T_{max,\,41}$ and varied with the density of Brønsted acid sites. However, it was less influenced by the density of the Lewis acid sites. In the case of $x$SZ(600) catalysts, the same relationship between formic acid conversion and Brønsted acidity was observed. The decrease in formic acid conversion on $x$SZ(600) catalysts with $x$ > 15 corresponded to a decrease in the BET surface area and an increase in the pyrosulfate proportion (Table 1 and Figure 2). This is also in line with the reduction of Zr–OH species, which is closely related to the structure of bridging bidentate sulfate species, observed on XPS (Figure 4 and Supplementary Figure S8) and IR (Figure 3). To understand the reaction mechanism of formic acid dehydration over the SZ catalyst, an on–off cycle test was conducted at 260 °C, using the most active 10SZ(600) catalyst (Figure 9). Notably, a sharp increase in the CO ($m/z$ = 28) and ·HCO ($m/z$ = 29) fragments was observed from the onset of the reaction, while the evolution of $\cdot H_2O$ ($m/z$ = 18) was delayed by approximately 1 min. This represents the transformation of Type I tridentate sulfates to Type II bridging bidentate species (Brønsted acids) by reacting with the water produced during formic acid dehydration. The protonated formic acid on a strong Brønsted acid site liberates water molecules at 100−150 °C, and the remaining charged acyl moiety $(O{=}CH)^+$ transforms into CO and surface OH group by interacting with nucleophilic oxygen in sulfate species [62]. In addition, after the formic acid injection was turned off, the intensities of the mass signals for ·CO and ·HCO decreased successively. However, the intensity of the mass signal for $H_2O$ slowly decreased and became invisible after 15 min, indicating strong adsorption of

water on the SZ catalyst. This can be indirect evidence of Brønsted acid generation by the reaction of tridentate sulfates with the produced water.

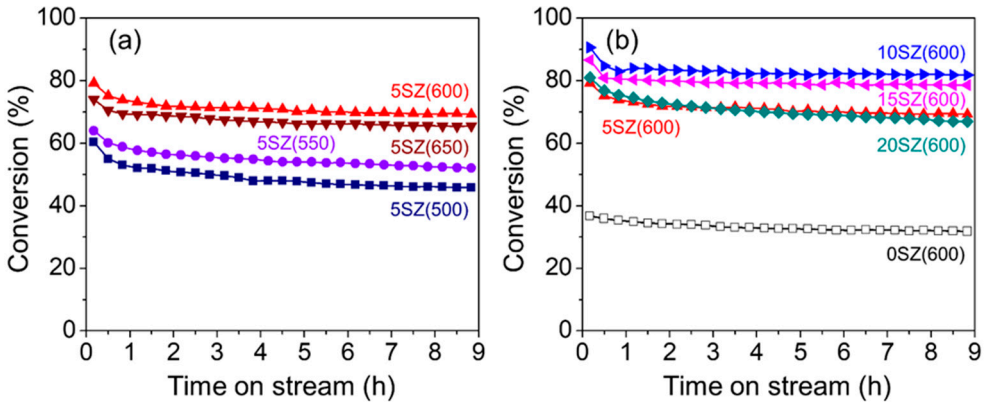


**Figure 7.** Formic acid conversion as a function of time on stream over (**a**) 5SZ(*y*) and (**b**) *x*SZ(600) catalysts at 260 °C and 6.0 $h^{-1}$ WHSV.

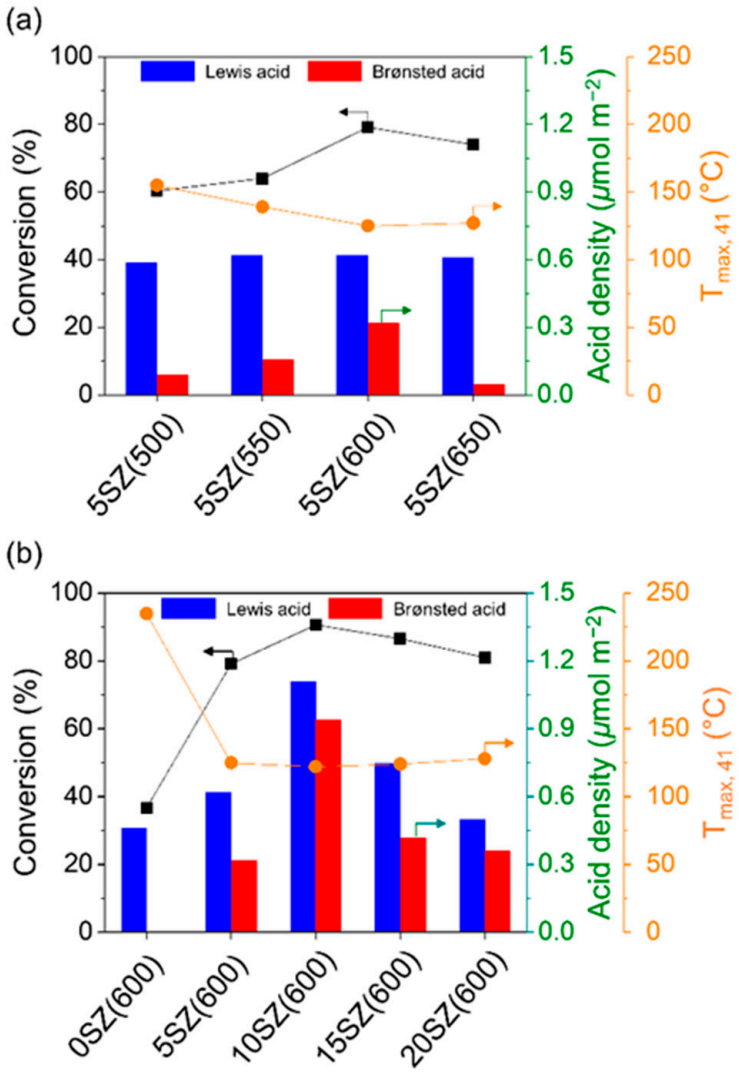


**Figure 8.** Correlation between formic acid conversion and Brønsted and Lewis acid densities, as well as $T_{max,\,41}$ over (**a**) 5SZ(*y*) and (**b**) *x*SZ(600) catalysts.

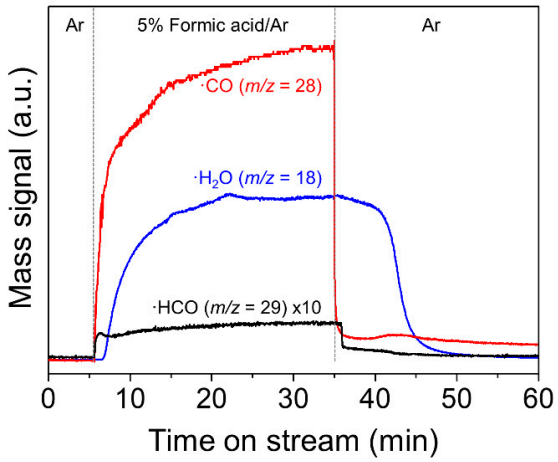


**Figure 9.** Evolution of ·$H_2O$ (*m*/*z* = 18), CO (*m*/*z* = 28), and ·HCO (*m*/*z* = 29) in mass spectra as a function of time on stream over 10SZ(600) catalyst during formic acid on–off cycle test at 260 °C and 6.0 $h^{-1}$ WHSV.

## 4. Conclusions

Two series of SZ, prepared by varying the calcination temperature and sulfate loading, were applied as catalysts for the dehydration of formic acid to carbon monoxide. Different sulfate species on the SZ catalysts, such as tridentate, bridging bidentate, and pyrosulfate, were identified by using TPDE, FTIR, and XPS analyses. The acidic properties of the SZ catalysts measured by Py-IR and IPA-TPD were correlated with the catalytic activity for formic acid dehydration. The conversion of formic acid on the SZ catalysts was more dependent on the Brønsted acidity, which is represented by the acid density and $T_{max,\ 41}$. The formation of pyrosulfate species on SZ catalysts with high sulfate loading (>15%) was found to have a detrimental effect on acidity and catalytic activity. The optimal calcination temperature and sulfate loading for the SZ catalysts with the highest CO yields were 600 °C and 10 wt.%, respectively. The overall results of this study suggest optimal preparation conditions for catalysts yielding high-purity CO from formic acid dehydration.

**Supplementary Materials:** The following supporting information can be downloaded at https://www.mdpi.com/article/10.3390/nano12173036/s1. Figure S1: Scanning electron microscope (SEM) images of 5SZ(*y*) catalysts. Figure S2: Pore size distribution of (a) 5SZ(*y*) and (b) *x*SZ(600) catalysts calculated from the desorption branch. Figure S3: Scanning electron microscope–energy-dispersive X-ray spectroscopy (SEM–EDS) images of 5SZ(600) catalyst. Figure S4: Thermogravimetric analysis profiles of (a) 5SZ(*y*) and (b) *x*SZ(600) catalysts. Figure S5: SEM images of *x*SZ(600) catalysts. Figure S6: Evolution of ·NH (*m*/*z* = 15), ·$H_2O$ (*m*/*z* = 18), and $SO_2$ (*m*/*z* = 64) in mass spectra as a function of temperature during temperature-programmed decomposition of as-prepared 10SZ (solid line) and calcined 10SZ(600) (dashed line) catalysts. Figure S7: FTIR spectra of (a) 5SZ(*y*) and (b) *x*SZ(600) in the range of 2000–4000 $cm^{-1}$. Figure S8: Deconvoluted O 1s XPS spectra for (a) 5SZ(*y*) and (b) *x*SZ(600) catalysts. Figure S9: Evolution of ·$CH_3CO$ (*m*/*z* = 43) and ·$C_3H_5$ (*m*/*z* = 41) in mass spectra as a function of temperature during IPA-TPD of 0SZ(600). Figure S10: Formic acid conversion as a function of time on stream over 10SZ(*y*) catalysts at 260 °C and 6.0 $h^{-1}$ WHSV.

**Author Contributions:** H.J.L., D.-C.K. and E.-J.K., data curation, formal analysis, investigation, and writing—original draft; Y.-W.S., methodology and validation; D.-P.K., resources, project administration, and funding acquisition; H.H. and H.-K.M., conceptualization, supervision, and writing—review and editing. All authors have read and agreed to the published version of the manuscript.

**Funding:** This work was supported by the C1 Gas Refinery Program (2015M3D3A1A01064899) and the Carbon to X Program (2020M3H7A1098273) through the National Research Foundation of Korea (NRF) funded by the Ministry of Science and ICT of the Korean government.

**Institutional Review Board Statement:** Not applicable.

**Informed Consent Statement:** Not applicable.

**Data Availability Statement:** Not applicable.

**Conflicts of Interest:** The authors declare that they have no known competing financial interests or personal relationships that could have appeared to influence the work reported in this paper.

## References


1. Omori, N.; Matsuo, H.; Watanabe, S.; Puschmann, M. Influence of carbon monoxide gas on silicon dioxide dry etching. *Surf. Sci.* **1996**, *352–354*, 988–992. [CrossRef]
2. Bengt, J.N.; Claus, F.P. A Process for the Preparation of Ultra-High Purity Carbon Monoxide. EP Patent 3031956 A1, 16 June 2016.
3. Yang, J. Method for Industrially Preparing High-Purity Carbon Monoxide through Formic Acid Dehydration. CN Patent 105084359A, 25 November 2015.
4. Kwon, S.; Lin, T.C.; Iglesia, E. Formic acid dehydration rates and elementary steps on Lewis acid–base site pairs at anatase and rutile $TiO_2$ surfaces. *J. Phys. Chem. C* **2020**, *124*, 20161–20174. [CrossRef]
5. Yu, W.-Y.; Mullen, G.M.; Flaherty, D.W.; Mullins, C.B. Selective hydrogen production from formic acid decomposition on Pd–Au bimetallic surfaces. *J. Am. Chem. Soc.* **2014**, *136*, 11070–11078. [CrossRef] [PubMed]
6. Al-Nayili, A.; Majdi, H.S.; Albayati, T.M.; Saady, N.M.C. Formic acid dehydrogenation using noble-metal nanoheterogeneous catalysts: Towards sustainable hydrogen-based energy. *Catalysts* **2022**, *12*, 324. [CrossRef]
7. Léval, A.; Agapova, A.; Steinlechner, C.; Alberico, E.; Junge, H.; Beller, M. Hydrogen production from formic acid catalyzed by a phosphine free manganese complex: Investigation and mechanistic insights. *Green Chem.* **2020**, *22*, 913–920. [CrossRef]
8. Singh, A.K.; Singh, S.; Kumar, A. Hydrogen energy future with formic acid: A renewable chemical hydrogen storage system. *Catal. Sci. Technol.* **2016**, *6*, 12–40. [CrossRef]
9. Eppinger, J.; Huang, K.-W. Formic acid as a hydrogen energy carrier. *ACS Energy Lett.* **2016**, *2*, 188–195. [CrossRef]
10. Mihet, M.; Dan, M.; Barbu-Tudoran, L.; Lazar, M.D.; Blanita, G. Controllable $H_2$ generation by formic acid decomposition on a novel Pd/templated carbon catalyst. *Hydrogen* **2020**, *1*, 22–37. [CrossRef]
11. Lee, H.J.; Kang, D.-C.; Pyen, S.H.; Shin, M.; Suh, Y.-W.; Han, H.; Shin, C.-H. Production of $H_2$-free CO by decomposition of formic acid over $ZrO_2$ catalysts. *Appl. Catal. A* **2017**, *531*, 13–20. [CrossRef]
12. Pyen, S.; Hong, E.; Shin, M.; Suh, Y.-W.; Shin, C.-H. Acidity of co-precipitated $SiO_2$-$ZrO_2$ mixed oxides in the acid-catalyzed dehydrations of iso-propanol and formic acid. *Mol. Catal.* **2018**, *448*, 71–77. [CrossRef]
13. Tanabe, K. Surface and catalytic properties of $ZrO_2$. *Mater. Chem. Phys.* **1985**, *13*, 347–364. [CrossRef]
14. Jung, K.T.; Bell, A.T. The effects of synthesis and pretreatment conditions on the bulk structure and surface properties of zirconia. *J. Mol. Catal. A* **2020**, *163*, 27–42. [CrossRef]
15. Miyata, H.; Kohno, M.; Ono, T.; Ohno, T.; Hatayama, F. FTIR-investigation of reaction of 2-propanol and acidity of vanadium oxides layered on zirconia and their surface structure. *J. Mol. Catal.* **1990**, *63*, 181–191. [CrossRef]
16. Kim, T.W.; Kim, C.; Jeong, H.; Shin, C.-H.; Suh, Y.-W. Hydrogen storage into monobenzyltoluene over Ru catalyst supported on $SiO_2$-$ZrO_2$ mixed oxides with different Si/Zr ratios. *Korean J. Chem. Eng.* **2020**, *37*, 1427–1435. [CrossRef]
17. Lee, J.-H.; Shin, C.-H.; Suh, Y.-W. Higher Brønsted acidity of $WO_x/ZrO_2$ catalysts prepared using a high-surface-area zirconium oxyhydroxide. *Mol. Catal.* **2017**, *438*, 272–279. [CrossRef]
18. Oki, H.; Morita, T.; Nakajima, K.; Hara, M. $MoO_3/ZrO_2$ as a stable, reusable, and highly active solid acid catalyst for polyester polyol synthesis. *Chem. Lett.* **2013**, *42*, 1314–1316. [CrossRef]
19. Annuar, N.H.R.; Jalil, A.A.; Triwahyono, S.; Fatah, N.A.A.; Teh, L.P.; Mamat, C.R. Cumene cracking over chromium oxide zirconia: Effect of chromium(VI) oxide precursors. *Appl. Catal. A* **2014**, *475*, 487–496. [CrossRef]
20. Resofszki, G.; Muhler, M.; Sprenger, S.; Wild, U.; Paál, Z. Electron spectroscopy of sulfated zirconia, its activity in n-hexane conversion and possible reasons of its deactivation. *Appl. Catal. A* **2003**, *240*, 71–81. [CrossRef]
21. Chen, G.; Guo, C.-Y.; Qiao, H.; Ye, M.; Qiu, X.; Yue, C. Well-dispersed sulfated zirconia nanoparticles as high-efficiency catalysts for the synthesis of bis(indolyl)methanes and biodiesel. *Catal. Commun.* **2013**, *41*, 70–74. [CrossRef]
22. Yusoff, M.H.M.; Abdullah, A.Z. Effects of zirconia loading in sulfated zirconia/SBA-15 on esterification of palmitic acid with glycerol. *Korean J. Chem. Eng.* **2018**, *35*, 383–393. [CrossRef]
23. Matsuhashi, H.; Nakamura, H.; Ishihara, T.; Iwamoto, S.; Kamiya, Y.; Kobayashi, J.; Kubota, Y.; Yamada, T.; Matsuda, T.; Matsushita, K.; et al. Characterization of sulfated zirconia prepared using reference catalysts and application to several model reactions. *Appl. Catal. A* **2009**, *360*, 89–97. [CrossRef]
24. Katada, N.; Tsubaki, T.; Niwa, M. Characterization of sulfated zirconia prepared using reference catalysts and application to several model reactions. Measurements of number and strength distribution of Brønsted and Lewis acid sites on sulfated zirconia by ammonia IRMS–TPD method. *Appl. Catal. A* **2008**, *340*, 76–86. [CrossRef]
25. Huang, D.; Chen, S.; Ma, S.; Chen, X.; Ren, Y.; Wang, M.; Ye, L.; Zhang, L.; Chen, X.; Liu, Z.-P.; et al. Determination of acid structures on the surface of sulfated monoclinic and tetragonal zirconia through experimental and theoretical approaches. *Catal. Sci. Technol.* **2022**, *12*, 596–605. [CrossRef]
26. Song, X.; Sayari, A. Sulfated zirconia-based strong solid-acid catalysts: Recent progress. *Catal. Rev.* **1996**, *38*, 329–412. [CrossRef]

27. Emeis, C.A. Determination of integrated molar extinction coefficients for infrared absorption bands of pyridine adsorbed on solid acid catalysts. *J. Catal.* **1993**, *141*, 347–354. [CrossRef]
28. Ward, D.A.; Ko, E.I. One-step synthesis and characterization of zirconia-sulfate aerogels as solid superacids. *J. Catal.* **1994**, *150*, 18–33. [CrossRef]
29. Budd, M.I. Sintering and crystallization of a glass powder in the MgO-$Al_2O_3$-$SiO_2$-$ZrO_2$ system. *J. Mater. Sci.* **1993**, *28*, 1007–1014. [CrossRef]
30. Cassiers, K.; Linssen, T.; Aerts, K.; Cool, P.; Lebedev, O.; Van Tendeloo, G.; Van Grieken, R.; Vansant, E.F. Controlled formation of amine-templated mesostructured zirconia with remarkably high thermal stability. *J. Mater. Chem.* **2003**, *13*, 3033–3039. [CrossRef]
31. Xia, Q.-H.; Hidajat, K.; Kawi, S. Effect of $ZrO_2$ loading on the structure, acidity, and catalytic activity of the $SO_4^{2-}$/$ZrO_2$/MCM-41 acid catalyst. *J. Catal.* **2002**, *205*, 318–331. [CrossRef]
32. Joo, J.B.; Vu, A.; Zhang, Q.; Dahl, M.; Gu, M.; Zaera, F.; Yin, Y. A sulfated $ZrO_2$ hollow nanostructure as an acid catalyst in the dehydration of fructose to 5-hydroxymethylfurfural. *ChemSusChem* **2013**, *6*, 2001–2008. [CrossRef] [PubMed]
33. Zhang, X.; Rabee, A.I.M.; Isaacs, M.; Lee, A.F.; Wilson, K. Sulfated zirconia catalysts for D-sorbitol cascade cyclodehydration to isosorbide: Impact of zirconia phase. *ACS Sustain. Chem. Eng.* **2018**, *6*, 14704–14712. [CrossRef]
34. Witoon, T.; Permsirivanich, T.; Kanjanasoontorn, N.; Akkaraphataworn, C.; Seubsai, A.; Faungnawakij, K.; Warakulwit, C.; Chareonpanich, M.; Limtrakul, J. Direct synthesis of dimethyl ether from $CO_2$ hydrogenation over Cu–ZnO–$ZrO_2$/$SO_4^{2-}$–$ZrO_2$ hybrid catalysts: Effects of sulfur-to-zirconia ratios. *J. Catal. Sci. Technol.* **2015**, *5*, 2347–2357. [CrossRef]
35. Katada, N.; Endo, J.-I.; Notsu, K.-I.; Yasunobu, N.; Naito, N.; Niwa, M. Superacidity and catalytic activity of sulfated zirconia. *J. Phys. Chem. B* **2000**, *104*, 10321–10328. [CrossRef]
36. Bensitel, M.; Saur, O.; Lavalley, J.-C.; Morrow, B.A. An infrared study of sulfated zirconia. *Mater. Chem. Phys.* **1988**, *19*, 147–156. [CrossRef]
37. Morterra, C.; Cerrato, G.; Emanuel, C.; Bolis, V. On the surface acidity of some sulfate-doped $ZrO_2$ catalysts. *J. Catal.* **1993**, *142*, 349–367. [CrossRef]
38. Glover, T.G.; Peterson, G.W.; DeCoste, J.B.; Browe, M.A. Adsorption of ammonia by sulfuric acid treated zirconium hydroxide. *Langmuir* **2012**, *28*, 10478–10487. [CrossRef]
39. Halstead, W.D. Thermal decomposition of ammonium sulphate. *J. Appl. Chem.* **1970**, *20*, 129–132. [CrossRef]
40. Reddy, B.M.; Patil, M.K. Organic syntheses and transformations catalyzed by sulfated zirconia. *Chem. Rev.* **2009**, *109*, 2185–2208. [CrossRef]
41. Yadav, G.D.; Nair, J.J. Sulfated zirconia and its modified versions as promising catalysts for industrial processes. *Microporous Mesoporous Mater.* **1999**, *33*, 1–48. [CrossRef]
42. Rabee, A.I.M.; Mekhemer, G.A.H.; Osatiashtiani, A.; Isaacs, M.A.; Lee, A.F.; Wilson, K.; Zaki, M.I. Acidity-reactivity relationships in catalytic esterification over ammonium sulfate-derived sulfated zirconia. *Catalysts* **2017**, *7*, 204. [CrossRef]
43. Hino, M.; Kurashige, M.; Matsuhashi, H.; Arata, K. The surface structure of sulfated zirconia: Studies of XPS and thermal analysis. *Thermochim. Acta* **2006**, *441*, 35–41. [CrossRef]
44. Marlowe, J.; Acharya, S.; Zuber, A.; Tsilomelekis, G. Characterization of sulfated $SnO_2$-$ZrO_2$ catalysts and their catalytic performance on the tert-butylation of phenol. *Catalysts* **2020**, *10*, 726. [CrossRef]
45. Mishra, M.K.; Tyagi, B.; Jasra, R.V. Synthesis and characterization of nano-crystalline sulfated zirconia by sol–gel method. *J. Mol. Catal. A* **2004**, *223*, 61–65. [CrossRef]
46. Deshmane, V.G.; Adewuyi, Y.G. Mesoporous nanocrystalline sulfated zirconia synthesis and its application for FFA esterification in oils. *Appl. Catal. A* **2013**, *462–463*, 196–206. [CrossRef]
47. Vargas, D.A.; Méndez, L.J.; Cánepa, A.S.; Bravo, R.D. Sulfated airconia: An efficient and reusable heterogeneous catalyst in the Friedel–Crafts acylation reaction of 3-methylindole. *Catal. Lett.* **2017**, *147*, 1496–1502. [CrossRef]
48. Patel, S.B.; Baker, N.; Marques, I.; Hamlekhan, A.; Mathew, M.T.; Takoudis, C.; Friedrich, C.; Sukotjo, C.; Shokuhfar, T. Transparent $TiO_2$ nanotubes on zirconia for biomedical applications. *RSC Adv.* **2017**, *7*, 30397–30410. [CrossRef]
49. Rammal, M.B.; Omanovic, S. Synthesis and characterization of NiO, $MoO_3$, and $NiMoO_4$ nanostructures through a green, facile method and their potential use as electrocatalysts for water splitting. *Mater. Chem. Phys.* **2020**, *255*, 123570. [CrossRef]
50. Walrafen, G.E.; Irish, D.E.; Young, T.F. Raman spectral studies of molten potassium bisulfate and vibrational frequencies of $S_2O_7$ groups. *J. Chem. Phys.* **1962**, *37*, 662–670. [CrossRef]
51. Woo, J.-C.; Kim, S.-G.; Koo, J.-G.; Kim, G.-H.; Kim, D.-P.; Yu, C.-H.; Kang, J.-Y.; Kim, C.-I. A study on dry etching for profile and selectivity of $ZrO_2$ thin films over Si by using high density plasma. *Thin Solid Films* **2009**, *517*, 4246–4250. [CrossRef]
52. Tan, J.; He, X.; Yin, F.; Liang, X.; Li, G. Post-synthetic Ti exchanged UiO-66-$NH_2$ metal-organic frameworks with high faradaic efficiency for electrochemical nitrogen reduction reaction. *Int. J. Hydrog. Energy* **2021**, *46*, 31647–31658. [CrossRef]
53. Huang, C.; Tang, Z.; Zhang, Z. Differences between zirconium hydroxide ($Zr(OH)_4 \cdot nH_2O$) and hydrous zirconia ($ZrO_2 \cdot nH_2O$). *J. Am. Ceram. Soc.* **2001**, *84*, 1637–1638. [CrossRef]
54. Mozalev, A.; Pytlicek, Z.; Kamnev, K.; Prasek, J.; Gispert-Guirado, F.; Llobet, E. Zirconium oxide nanoarrays via the self-organized anodizing of Al/Zr bilayers on substrates. *Mater. Chem. Front.* **2021**, *5*, 1917–1931. [CrossRef]
55. Yan, G.X.; Wang, A.; Wachs, I.E.; Baltrusaitis, J. Critical review on the active site structure of sulfated zirconia catalysts and prospects in fuel production. *Appl. Catal. A.* **2019**, *572*, 210–225. [CrossRef]

56. Ghoreishi, K.B.; Yarmo, M.A. Sol-gel sulphated silica as a catalyst for glycerol acetylation with acetic acid. *J. Sci. Technol.* **2013**, *5*, 65–78. Available online: https://penerbit.uthm.edu.my/ojs/index.php/JST/article/view/520 (accessed on 29 August 2022).
57. Gondal, M.A.; Fasasi, T.A.; Baig, U.; Mekki, A. Effects of oxidizing media on the composition, morphology and optical properties of colloidal zirconium oxide nanoparticles synthesized via pulsed laser ablation in liquid technique. *J. Nanosci. Nanotechnol.* **2018**, *18*, 4030–4039. [CrossRef]
58. Ferrizz, R.M.; Gorte, R.J.; Vohs, J.M. TPD and XPS investigation of the interaction of $SO_2$ with model ceria catalysts. *Catal. Lett.* **2002**, *82*, 123–129. [CrossRef]
59. Zhang, L.; Hu, C.; Mei, W.; Zhang, J.; Cheng, L.; Xue, N.; Ding, W.; Chen, J.; Hou, W. Highly efficient sulfated Zr-doped titanoniobate nanoplates for the alcoholysis of styrene epoxide at room temperature. *Appl. Surf. Sci.* **2015**, *357*, 1951–1957. [CrossRef]
60. Gamliel, D.P.; Cho, H.J.; Fan, W.; Valla, J.A. On the effectiveness of tailored mesoporous MFI zeolites for biomass catalytic fast pyrolysis. *Appl. Catal. A* **2016**, *522*, 109–119. [CrossRef]
61. Chen, Y.-Y.; Chang, C.-J.; Lee, H.V.; Juan, J.C.; Lin, Y.-C. Gallium-immobilized carbon nanotubes as solid templates for the synthesis of hierarchical Ga/ZSM-5 in methanol aromatization. *Ind. Eng. Chem. Res.* **2019**, *58*, 7948–7956. [CrossRef]
62. Popova, G.Y.; Zakharov, I.I.; Andrushkevich, T.V. Mechanism of formic acid decomposition on P-Mo heteropolyacid. *React. Kinet. Catal. Lett.* **1999**, *66*, 251–256. [CrossRef]